Assessment of the effect of isolated porosity defects on the fatigue performance of additive manufactured titanium alloy

Biswal, R., Syed, A. & Zhang, X.

Original citation & hyperlink:
Biswal, R, Syed, A & Zhang, X 2018, 'Assessment of the effect of isolated porosity defects on the fatigue performance of additive manufactured titanium alloy' Additive Manufacturing, vol. 23, pp. 433-442.
https://dx.doi.org/10.1016/j.addma.2018.08.024

DOI 10.1016/j.addma.2018.08.024
ISSN 2214-7810
ESSN 2214-8604
Publisher: Elsevier

Assessment of the effect of isolated porosity defects on the fatigue performance of additive manufactured titanium alloy

Romali Biswal, Abdul Khadar Syed, Xiang Zhang*

Research Centre for Manufacturing and Materials Engineering, Coventry University, Coventry, CV1 5FB, UK

* Corresponding authors;
Email addresses: biswalr@uni.coventry.ac.uk; abdul.khadar@coventry.ac.uk; xiang.zhang@coventry.ac.uk

Abstract

Studies on additive manufactured (AM) materials have shown that porosity reduces the fatigue strength. However, the quantitative impact is not well understood. This paper presents a mechanistic approach to quantify the influence of size, location and shape of gas pores on the fatigue strength of AM Ti-6Al-4V. Ideal spherical and oblate spherical pore geometries were used in the finite element (FE) analysis. The FE results showed a stress concentration factor of 2.08 for an internal spherical pore, 2.1 for a surface hemispherical pore and 2.5 for an internal oblate spherical pore. Subsurface pores within a distance of the pore diameter from the free surface were found to be most critical. The material's constitutive relation under the cyclic load was modelled by a mixed non-linear hardening rule that was calibrated with published literature on selective laser melted Ti-6Al-4V. The cyclic plasticity effect caused a local mean stress relaxation, which was found to be dependent on the pore geometry, the applied stress amplitude and the stress ratio. Fatigue life was predicted by using the FE calculated local strain amplitude and maximum stress in the strain-life relationship proposed by Smith-Watson-Topper. The methodology was validated by published literature with crack initiation at gas pores of known size, location, and shape. Parametric study showed that for internal pores, fatigue performance is more sensitive to the shape and location of the pore than the size. An S-N curve was proposed by the parametric study to account for the fatigue strength reduction due to internal gas pores.

Keywords: Porosity defects; stress concentration factor; additive manufactured Ti-6Al-4V; finite element modelling; fatigue life prediction.

1. Introduction

Additive manufacturing (AM) offers unprecedented design freedom, material savings and ease of process automation that makes it a key technology in the industry 4.0 revolution. Consequently, AM is being rapidly researched for industrial applications involving components made from nickel, titanium, stainless steel and aluminium alloys [1,2]. Particularly, aerospace applications require a high strength to weight ratio, and the use of AM processed titanium parts can potentially reduce the weight of the component to half of the conventionally machined component [3]. However, studies have shown that the process-induced defects in as-built AM parts have a detrimental influence on the fatigue performance [4–7]. These defects are of two types, (a) lack of fusion (LOF) defects, in the form of irregular and flat delaminations and (b) gas pores, in the form of spherical or near-spherical gas pockets.

Powder bed fusion, such as selective laser melting (SLM) and electron beam melting (EBM), and directed energy deposition techniques, such as direct laser deposition (DLD), have a higher propensity towards porosity inclusion. Porosity volume fractions in AM Ti-6Al-4V built with optimized processing parameters are reported between 0.08% - 0.23% for SLM [8, 9], 0.03 - 0.19% for EBM [10,11] and 0.013% - 0.36% for DLD process [12]. Post-processing techniques such as hot isostatic pressing (HIPing) have been reported to be very effective in reducing the size of gas pores, but owing to the internal pressure, gas pores cannot be eliminated [10].

Statistical models developed through mechanical testing [13] show a strong correlation between the static strength and fatigue limit of AlSi10Mg in the presence of internal defects. However, the results cannot be transferred directly to Ti-6Al-4V due to a large difference in the microstructure and mechanical properties of the two alloys. Existing empirical models account for the effect of porosity on the fatigue performance by determining the reduced fatigue limit on the basis of the projected area of the defect on the plane perpendicular to the loading axis [7,14]. According to one such model, known as Murakami's model [15], fatigue limit can be expressed as a function of the defect location (using a correlation co-efficient), the defect size (using the square root of the projected area) and the material's Vicker's hardness. This approach worked for irregular LOF defects (similar to cracks) in AM Ti-6Al-4V [7,16] but gave a highly conservative prediction for specimens with gas pores [14]. The near-spherical geometry of gas pores indicate that the behaviour may be more accurately predicted by using the notch fatigue approach and crack initiation based models. Realistic crack initiation models can be built with inputs from advanced techniques such as X-ray computed tomography (X-ray CT), which map the porosity distribution to include the shape, size and location details. Consequently, the stress concentration factor value at individual defects can be computed by converting these 3-D maps into finite element models. In a study [17], the authors used X-ray CT to develop a static finite element model and concluded that stress concentration factor for pores can be expressed as a function of a porosity characteristic parameter, which was defined as the ratio of pore diameter to its distance to the free surface. However, this parameter did not include the shape of the porosity defect. Stress concentration factor obtained by this approach was found to be of lower value than the theoretical stress concentration factor value at a spherical cavity in an infinitely large body [18], and therefore, may not be applicable for gas pores.

Published S-N data of SLM, EBM and DLD Ti-6Al-4V show that unpolished specimens performed poorly with no measurable effect of any post processing, while the fatigue strength was increased by a factor of 2 to 3 for the specimens tested with a polished surface [5,16,19]. In polished specimens, heat treatment (without HIPing) did not show any significant improvement in fatigue performance as compared to non-heat treated specimens [20–22], indicating that for machined (polished) specimens internal porosity dominates the fatigue performance more than the microstructure. Fatigue performance of HIPed AM specimens was found to be better than wrought Ti-6Al-4V [8, 15–18]. Nonetheless, post-processing will increase the production time and cost. Furthermore, in [10] it was found that gas pores reduced by HIPing to below the X-ray CT detectable limit of 5.2 µm subsequently underwent regrowth when the material was exposed to temperatures at above 1000°C.

This can be due to the coupled effect of an increase in the internal pressure in the gas pore and the simultaneous recrystallization of the surrounding microstructure above the β transus temperature.

This study is focused on the effect of gas pores on the fatigue performance by developing a fatigue life prediction method for AM Ti-6Al-4V. Microstructural influence on fatigue crack initiation was considered via. (1) a cyclic plasticity model to calculate the material response in the plastic deformation regime, and (2) using the AM Ti-6Al-4V material parameters in the strain-life relation. Published cyclic stress-strain and strain-life data of SLM, EBM and DLD Ti-6Al-4V were used to establish representative relationships for powder-based AM processes. A cyclic plasticity model was calibrated by using the stabilized cyclic stress-strain curve for AM Ti-6Al-4V, thereby accounting for the effect of microstructure on the calculated local stress and strain histories at the pore. Finally, the calculated local strain amplitude and maximum stress at the root of the pore was used in the strain-life relation with the Smith-Watson-Topper (SWT) model to account for the mean stress effect on the predicted fatigue life for different pore geometries. The fatigue life prediction method was first validated by test data from the literature and then used to propose an S-N curve with gas pore effect.

2. Material properties

2.1 Cyclic stress-strain curve

Based on literature, SLM [26,27] and DLD Ti-6Al-4V [20] have very similar cyclic stress-strain relationship in comparison with the wrought material (Fig. 1), which led us to use a single cyclic stress-strain curve for the powder-based AM processed Ti-6Al-4V. Figure 1 also shows that AM Ti-6Al-4V is cyclic softening comparing to its monotonic stress-strain curve. In this research, the cyclic stress-strain curve used in the FE model was adopted from [26] and expressed in the Ramberg-Osgood relationship, Eq. (1).

$$\frac{\Delta\varepsilon}{2} = \frac{\Delta\sigma}{2E} + \left(\frac{\Delta\sigma}{2K'}\right)^{\frac{1}{n'}} \tag{1}$$

where $\Delta\varepsilon$ and $\Delta\sigma$ are the strain range and stress range, E the elastic modulus, K' the cyclic strength coefficient and n' the cyclic strain hardening exponent.

Use of laser and electron beam (high energy density heat sources) in SLM, DLD and EBM processes leads to rapid cooling rates (SLM between 10^4 and 10^6 °C/s [28], DLD and EBM between 10^3 and 10^4 °C/s [29,30]) while the cooling rate of wrought process lies between 10^{-2} and 10^2 °C/s [31]. Since the cooling rate controls the microstructure, this explains the similarity in the cyclic deformation behaviour between the SLM, DLD and EBM as compared to the wrought material. The width of the α lamellae in EBM and DLD is 1-3 µm [20,32] and that of martensite α' in SLM lies between 0.3-1 µm [33], whereas the α grain size reported for wrought material is 15-20 µm [34,35]. Application of cyclic loads prompts the material to undergo 'shakedown' during the initial few cycles, causing the dislocation substructure to rearrange with each cycle until a stable configuration is reached. When the applied stress is more than the yield strength of the material, the slip dislocations tend to pile up at the grain boundaries and at regions of high dislocation density which restricts any further dislocation movement through the lattice [36]. In other words, cyclic deformation behaviour is strongly dependent on the width of α grains in Ti-6Al-4V.

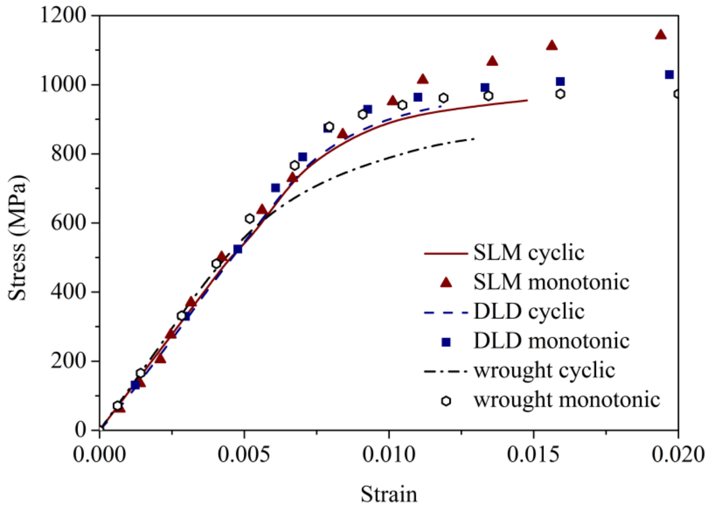

Fig. 1. Cyclic stress-strain curves of AM Ti-6Al-4V [20,26] compared with wrought Ti-6Al-4V [35].

2.2 S-N data for AM Ti-6Al-4V

Due to the unavoidable presence of internal defects in as-built powder-based AM Ti-6Al-4V, post-processed (HIPed) S-N data [8,22–25] was used as baseline for fatigue life prediction. Fig. 2 shows the S-N data of AM Ti-6Al-4V in comparison with the wrought material. The best-fit curve in terms of the stress amplitude was used against the reversals to failure ($2N_f$) on a logarithmic scale to estimate the material parameters for Basquin relation Eq. (2).

$$\frac{\Delta\varepsilon_e}{2} = \frac{\sigma'_f}{E}(2N_f)^b \tag{2}$$

where $\Delta\varepsilon_e$ is the elastic strain range, σ_f' the fatigue strength coefficient, $2N_f$ the load reversals to failure, and b the fatigue strength exponent.

The plastic strain component was calculated by using Eq. (1) and used against the reversals to failure on a logarithmic scale to obtain the material parameters for the Coffin-Manson relation (Eq. 3). HIPed AM Ti-6Al-4V was found to have better fatigue performance than wrought Ti-6Al-4V (annealed bar). This can be explained by the relatively fine lamellar microstructure and reduction in internal defects after HIPing treatment [37]. The summation of the elastic strain amplitude (Eq. 2) and plastic strain amplitude (Eq. 3) gives the total strain, ε, as shown in Eq. (4). The cyclic material property values for Eqs. 1-3 are given in Table 1.

$$\frac{\Delta\varepsilon_p}{2} = \varepsilon'_f(2N_f)^c \tag{3}$$

where $\Delta\varepsilon_p$ is the plastic strain range, ε'_f the fatigue ductility coefficient and c the fatigue ductility exponent.

$$\frac{\Delta\varepsilon}{2} = \frac{\sigma'_f}{E}(2N_f)^b + \varepsilon'_f(2N_f)^c \tag{4}$$

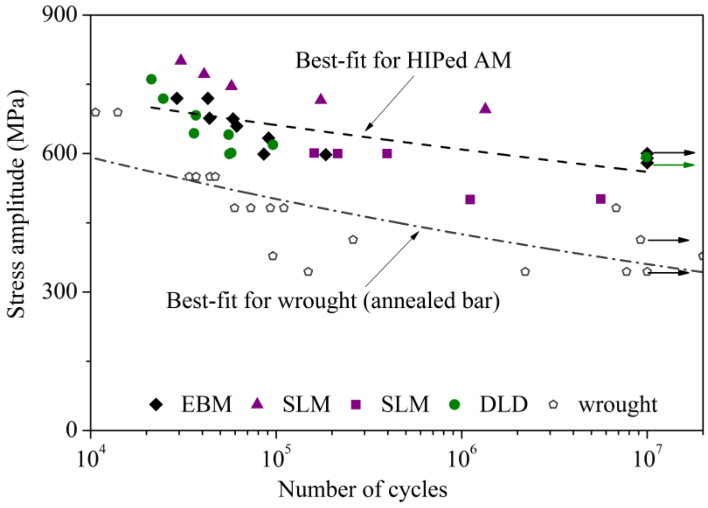

Fig. 2. S-N data of powder-based AM Ti-6Al-4V (loaded in the build direction, polished surface, hot isostatically pressed condition). Applied stress ratio $R = -1$, EBM [25], SLM [8,22], DLD [25] and wrought [38].

Table 1. Material parameters under cyclic load for powder AM Ti-6Al-4V based on the comparative study presented in Fig. 1 and Fig. 2.

Modulus of elasticity, E (GPa)	Cyclic strength coefficient K'(MPa)	Strain hardening exponent n'	Fatigue strength coefficient σ_f' (MPa)	Fatigue strength exponent b	Fatigue ductility coefficient ε_f'	Fatigue ductility exponent c
111	2085	0.186	1163	−0.046	0.043	−0.25

2.3 Porosity characterization in AM Ti-6Al-4V

Polished and etched (using Kroll's reagent) metallographic samples of SLM Ti-6Al-4V built with optimized processing parameters were studied under the scanning electron microscope. All the observed gas pores were in the size range of 5 to 100 µm diameter with an average diameter of 34 µm. The microstructure in the surrounding of the gas pores was similar to the overall microstructure, indicating no significant difference in the cooling rates in the vicinity of the pores. Fig. 3(a) and 3(b) show the different types of internal defects that were studied. The images indicate that the geometry of the defects can be assumed to be ideal spherical or oblate spherical for modelling purposes. The observed porosity morphology was in agreement with the porosity in the literature using optimised AM process characterised by X-ray CT[10], metallography [3] and fractography results [7].

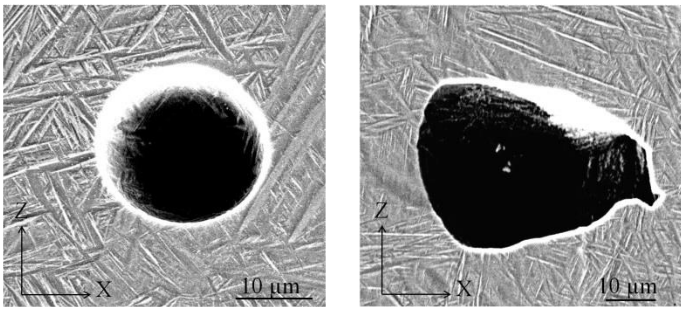

(a) (b)

Fig. 3. Porosity defects found in SLM Ti-6Al-4V specimens (a) spherical gas pore, (b) oblate spherical pore. Build direction is in Z axis.

3. FE modelling and life prediction method

3.1 Types of pores modelled and model assumptions

Based on the micrographs presented in the previous section, spherical and oblate spherical geometry was used to study the two extreme shapes of gas pores. Further, the effect of location was studied by assuming a subsurface spherical pore and a surface hemispherical pore. Fig. 4 illustrates the four different pore geometries modelled in this study. Elastic mechanical properties were assumed to be orthotropic with respect to the build direction.

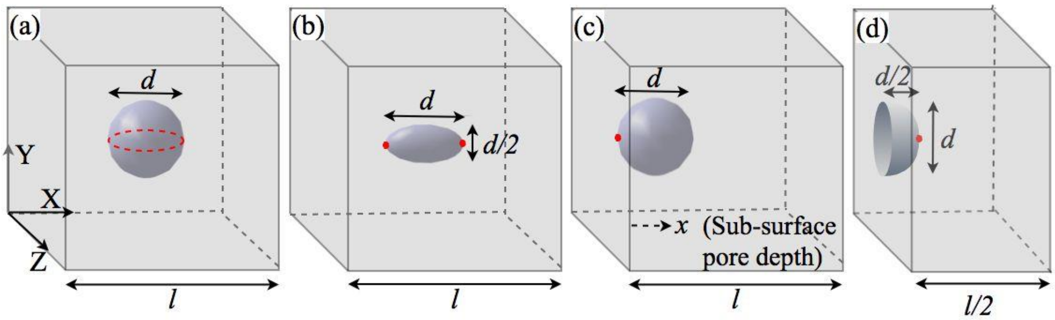

Fig. 4. Schematic of a cube containing one of the following pores, as used in the FE model, (a) internal spherical, (b) internal oblate spherical, (c) subsurface spherical (x is the distance from pore edge to surface), (d) surface hemispherical. Stress was applied on the Z-X plane and the red marks indicate the root of the pore where stress concentration is calculated.

3.2 Elastic stress analysis

Internal pores (spherical and oblate spherical) were modelled by using a ⅛ model with three planes of symmetry, and the subsurface spherical pore and surface hemispherical pore were modelled by a ¼ model with two planes of symmetry (X-Z, Y-X). FE mesh convergence analysis showed that a ratio of pore (major) diameter to finite element size of 25 is the required minimum mesh size around pore. Quadratic tetrahedron element of 10 nodes (C3D10) was used for meshing the geometry (Fig. 5).

Stress concentration factor, K_t, is the ratio of the local maximum elastic stress to the applied stress. It is a geometric parameter, hence can vary with the model dimensions. FE analysis was performed to determine the minimum size of the model to study an internal pore. The pore diameter was kept constant while increasing the side length of the model. It was found that when the model length was eight times of the pore diameter, K_t value stabilizes. This implies that beyond this ratio of porosity size to model size, the porosity size does not affect the computed results. This condition holds true for practical applications where the component dimension can be orders of magnitude greater than the size of porosity. It can also be inferred that a change in the size of internal pores does not affect the local stress and strain, and hence the fatigue crack initiation life.

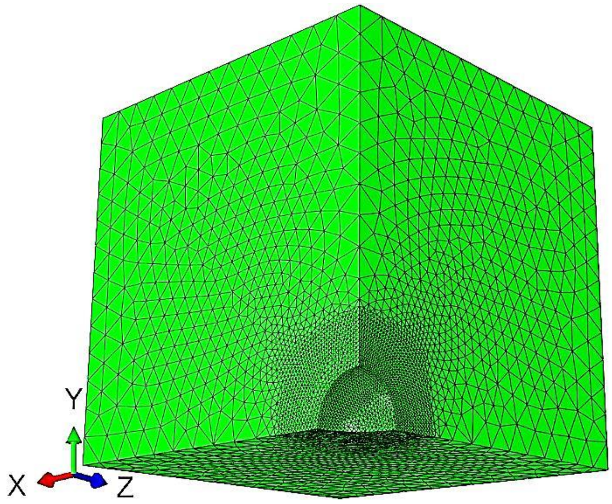

Fig. 5 FE mesh used for the internal spherical pore (1/8th of the geometry in Fig. 4a).

3.3 Elastic-plastic stress and strain analysis

Cyclic plasticity analysis was performed using the material models from ABAQUS library [39] to model the isotropic and kinematic softening of AM Ti-6Al-4V. The von Mises yield surface F is defined by Eq. (5).

$$F = f(\sigma - \alpha) - \sigma^0 \tag{5}$$

where f represents the von Mises stress function also referred to as the J_2 stress function, σ^0 is the yield stress and α the back-stress. The use of five back-stress components improves the fitting of stress-strain response of the model to the observed non-linear material response. The back-stress for each strain range is determined by integrating the back-stress evolution over the monotonically rising section of the stabilized hysteresis loop, as shown in Eq. (6) and the overall back-stress α, is the summation of these individual back-stresses, as shown in Eq. (7).

$$\alpha_{\mathrm{k}} = \frac{C_{\mathrm{k}}}{\gamma_{\mathrm{k}}}\left(1 - e^{-\gamma_{\mathrm{k}}\varepsilon^{\mathrm{pl}}}\right) + \alpha_{\mathrm{k},1} e^{-\gamma_k \varepsilon^{\mathrm{pl}}} \tag{6}$$

$$\alpha = \sum_{\mathrm{k}=1}^{N} \alpha_{\mathrm{k}} \tag{7}$$

where $\alpha_{\mathrm{k},1}$ is the k^{th} back-stress at the first data point (σ_1, 0), C_{k} the modulus in the plastic region, and γ_{k} the rate of decrease of the modulus with increasing plastic strain. These parameters were determined from inverse analysis operations to obtain a fit with stabilized hysteresis loop measured from experiment [26].

The isotropic softening behaviour of the model is introduced by Eq. (8).

$$\sigma^0 = \sigma_0 + Q_\infty \left(1 - e^{-b\bar{\varepsilon}^{pl}}\right), \tag{8}$$

where σ^0 is the yield stress for the n^{th} cycle, σ_0 the yield stress at zero plastic strain, Q_∞ the maximum change in the value of yield stress, b the rate of decrease of yield stress with an increase in equivalent plastic strain, $\bar{\varepsilon}^{pl}$. The FE model was calibrated such that the computed hysteresis loops reach the stabilized state within 20 load cycles. The values of C_{k}, γ_{k}, Q_∞ and b are given in Table 2.

The cyclic plasticity material model was validated with the experimentally measured hysteresis loops taken from [26]. Figure 6(a) compares the hysteresis curves of the first and the stabilized (200$^{\text{th}}$) cycle extracted from the experiment (at 2% fully reversed applied strain amplitude) [26] with the corresponding hysteresis loop calculated by the mixed cyclic plasticity model. Figure 6(b) shows the stabilized hysteresis loop for 1% and 2% fully reversed applied strain amplitudes, compared with the respective stabilized hysteresis loops computed by the model.

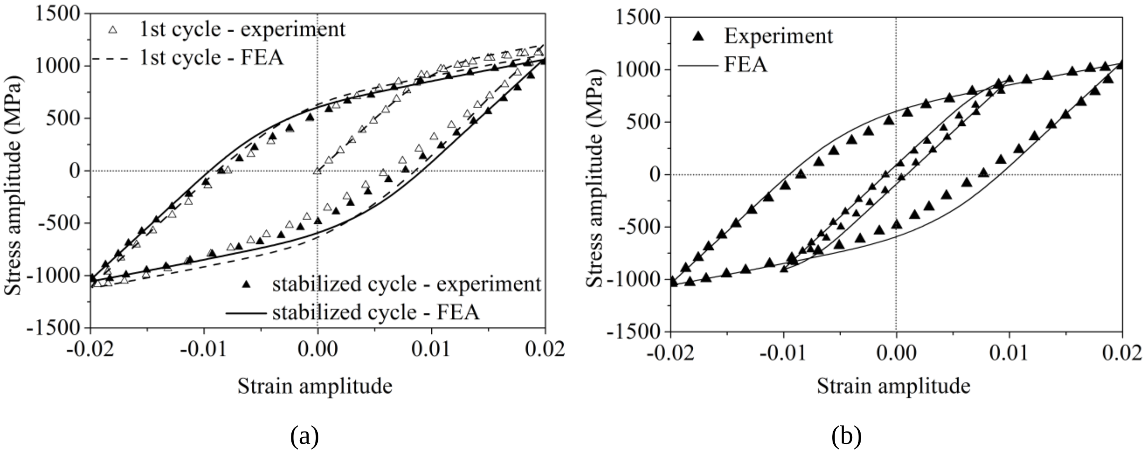

Fig. 6. (a) Comparison of the cyclic plasticity model results with experimental hysteresis loop [26] obtained at fully reversed applied strain amplitude of 2% for SLM Ti-6Al-4V ELI material, (b) 20th cycle of the cyclic plasticity model output for 1% and 2% applied strain amplitudes compared with the stabilized (200$^{\text{th}}$) hysteresis response from experiment [26].

Table 2. Elastic material properties and cyclic plasticity model parameters fitted to the stabilized hysteresis curves of SLM Ti-6Al-4V.

<table>
<tr><td colspan="12">Elastic properties, E_k, G_k (GPa) [26]</td></tr>
<tr><td colspan="2">E_1</td><td colspan="2">E_2</td><td colspan="2">E_3</td><td colspan="2">G_{12}</td><td colspan="2">G_{13}</td><td>G_{23}</td><td>υ_{ii}</td></tr>
<tr><td colspan="2">103.7</td><td colspan="2">95.238</td><td colspan="2">95.238</td><td colspan="2">35.966</td><td colspan="2">35.966</td><td>39.161</td><td>0.324</td></tr>
<tr><td colspan="12">Cyclic plasticity model parameters</td></tr>
<tr><td colspan="10">Kinematic model parameters, C_k (GPa), γ_k</td><td colspan="2">Isotropic model parameters, Q (MPa), b</td></tr>
<tr><td>C_1</td><td>γ_1</td><td>C_2</td><td>γ_2</td><td>C_3</td><td>γ_3</td><td>C_4</td><td>γ_4</td><td>C_5</td><td>γ_5</td><td>Q_∞</td><td>b</td></tr>
<tr><td>100</td><td>3000</td><td>70</td><td>3000</td><td>45</td><td>3000</td><td>30</td><td>850</td><td>29.7</td><td>12</td><td>−206</td><td>7</td></tr>
</table>

3.4 Neuber's approach as an alternative to FEA

If porosity is treated as a notch, then the Neuber's method can be applied to calculate the local stress and strain. Eq. (9) shows the relation between the local stress and strain amplitude (σ_a and ε_a) and the applied stress amplitude (S_a) and stress concentration factor (K_t). Since this approach is limited to applications with known analytical values of K_t, subsurface pores were not included in this analysis.

$$\sigma_a \varepsilon_a = \frac{(K_t S_a)^2}{E} \tag{9}$$

For life prediction, use of the fatigue notch strength reduction factor (K_f) is preferred over K_t to avoid highly conservative estimation (Eq. 10). K_f is the ratio of the fatigue strength of smooth specimens to that of notched specimens [40].

$$\sigma_a \varepsilon_a = \frac{(K_f S_a)^2}{E} \tag{10}$$

K_f and K_t are related by the notch sensitivity factor q, as shown in Eq. (11). From [41], the value of q for Ti-6Al-4V ELI can be deduced as 0.82. Therefore, K_f is lower than K_t to account for the plasticity and notch sensitivity effects.

$$K_f = q(K_t - 1) + 1 \tag{11}$$

Eq. (1) and Eq. (10) were solved simultaneously to obtain the local stress and total strain at the root of the pore.

3.5 Life prediction method

Fatigue life of AM Ti-6Al-4V containing a gas pore was predicted with the following assumptions:

(a) Pores can be considered as notches as they both are stress raisers, and fatigue life is controlled by the local stress and strains at the root of the critical pore (pore root location is indicated in Fig. 4).

(b) Predicted fatigue life at pore root using the local stress and strain values from FE model and material's S-N data represents the crack initiation life at pore root. (Note: subsequent crack propagation life is relatively short for a small specimen, whereas for a service part with a similar pore and subjected to similar local cyclic stress-strain histories, crack propagation life is much longer and cannot be neglected).

The cyclic plasticity model discussed in section 3.3 was used to obtain the stabilized local stress-strain response under fatigue loading. When the local stress-strain response is elastic (area enclosed by the hysteresis loop is negligible), the local stress amplitude can be used to predict the fatigue life by using the S-N data of HIPed AM Ti-6Al-4V as shown in Fig. 2. It should be noted that the local mean stress (if present) should be accounted by using Walker's equation [33] as shown in Eq. (12) because the data presented in Fig. 2 is at $R = -1$ (mean stress is zero).

$$\sigma_e = \sigma_{max} \left(\frac{1-R}{2} \right)^{0.28} \tag{12}$$

where σ_e is the equivalent maximum stress at $R = -1$, under the applied maximum stress, σ_{max}, and applied stress ratio, R.

When the local stress-strain response includes significant plastic deformation, the local strain should be used for fatigue life prediction. The local strain amplitude, ε_a, and the local maximum stress, σ_{max}, obtained from the cyclic plasticity model were used in the SWT model (Eq. 13) [42], where the local maximum stress term is used to account for the effect of the local mean stress.

$$\varepsilon_a \sigma_{max} = \frac{(\sigma'_f)^2}{E} (2N_f)^{2b} + \sigma'_f \, \varepsilon'_f \, (2N_f)^{b+c} \tag{13}$$

where the constants $\sigma_f{}'$ and $\varepsilon_f{}'$ are the fatigue strength and the fatigue ductility coefficients, b and c are the fatigue strength exponent and fatigue ductility exponent, respectively (values in Table 1).

4. Results and discussion

4.1 Stress concentration factor (K_t) for various pores

Values of K_t for the four different pore geometries were calculated from the elastic FE model with uniaxial loading condition using a Poisson's ratio of 0.324 [6]. It should be noted that Poisson's ratio, v, is an important parameter which affects the K_t in 3-D geometries. Elastic FE model results were validated by analytical solutions [18,43,44]. The results are presented in Table 3. It can be seen that K_t values are virtually the same for the internal spherical pore and the surface hemispherical pore. This is because that the "hot spot" at the surface pore root is subjected to a similar boundary condition as that of the internal pore. Fig. 7(a) shows that K_t continues to increase as the distance between the pore and the free surface is reduced below the pore diameter (d). In other words, location of the pore becomes critical if the porosity lies within a distance of d from the free surface. Figs. 7(b) and (c) show the stress distribution for subsurface pores under applied unit stress. Finally, for an internal oblate spherical pore (major diameter twice of minor diameter) K_t was also high, indicating that the shape of the pore is also an important factor in controlling the local stress concentration factor.

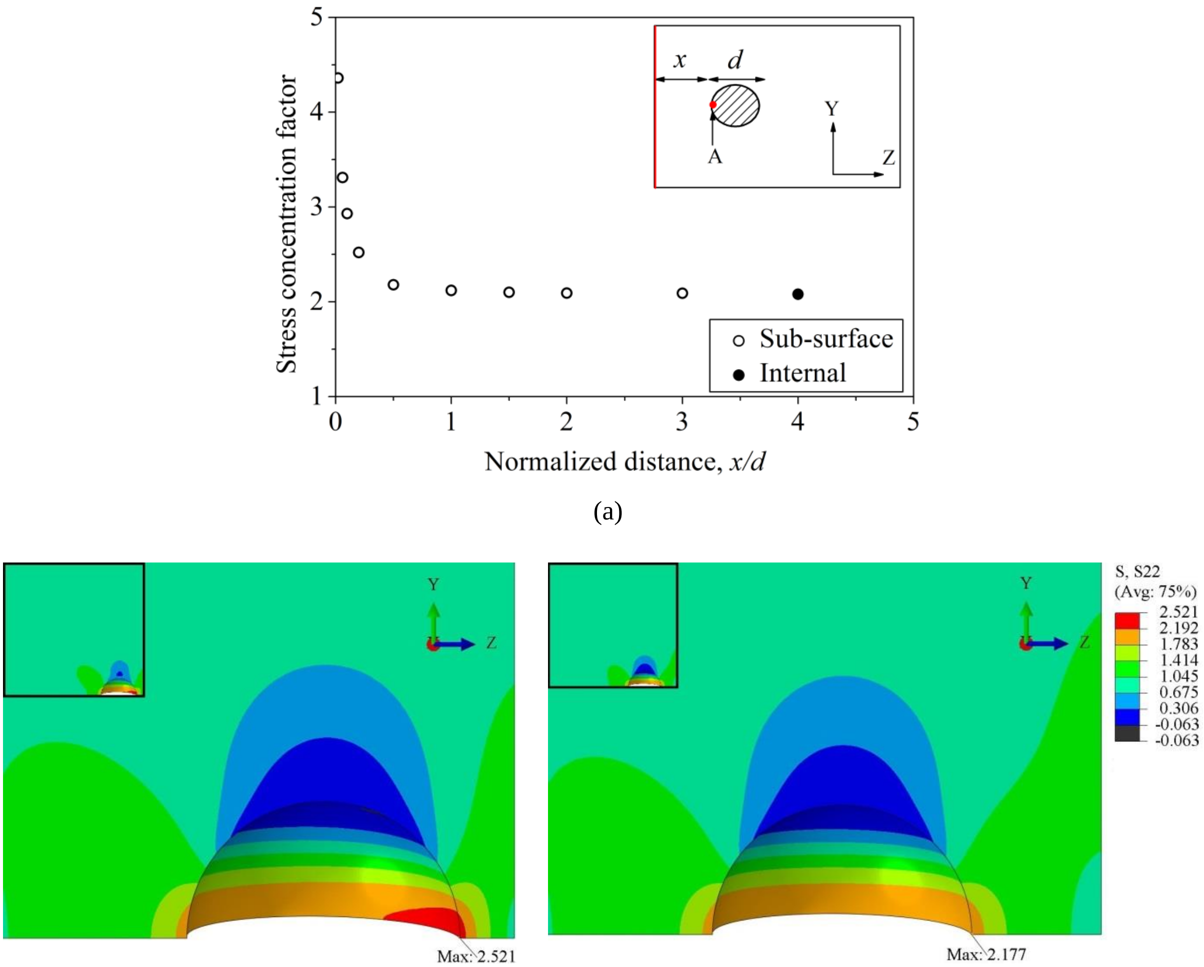

(a)

(b)

(c)

Fig. 7 Subsurface pore of diameter d: (a) stress concentration factor, K_t vs. distance, x to free surface (point A, marked in red), (b) and (c) overall model (top left corner) and enlarged view of local stress distribution under applied unit stress in the Z-X plane; $x = 0.2d$, K_t=2.52 in (b), $x = 0.5d$, K_t = 2.18 in (c).

Table 3. Stress concentration factor values obtained from elastic FE model for the studied pore geometries and comparison with published analytical solutions [18,43,44].

	Shape	Aspect ratio	Distance to surface	K_t	% error (FE vs. analytical solution)
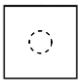	Spherical	1	4d	2.08	0.9
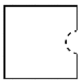	Hemispherical	1	Surface	2.1	0.6
	Oblate spherical	2	4d	2.5	1.2
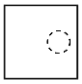	Subsurface	1	0.02d – 0.5d	4.36 - 2.18	N/A

4.2 Local stress and strains at porosity

(a) FE cyclic plasticity model

Elastic-plastic FEA was carried out on a specimen with an isolated pore to investigate the local stress-strain state, plastic deformation and local stress ratio at the root of the pore. The four different pore geometries shown in Table 3 were modelled and the specimen was subjected to a cyclic load with the maximum stress of 450 MPa, 600 MPa and 750 MPa, at applied stress ratios of 0.1, −0.2 and −0.5. The calibrated cyclic plasticity model (explained in section 3.3) was used to incorporate the cyclic stress-strain relationship in FEA. It was found that the mean stress at the root of the pore was always lower than the applied stress and the percentage reduction was directly proportional to the applied maximum stress, applied stress ratio, and the K_t. The local stress-strain response remained to be elastic dominant for the applied maximum stress of 450 MPa and 600 MPa with a stress ratio of 0.1, −0.2 and −0.5. When the applied maximum stress was increased to 750 MPa with a stress ratio of −0.5, significant cyclic plasticity was noticed. This behaviour can be due to the large stress amplitude in addition to the high applied maximum stress (nearly 80% of the yield stress), that causes the material within the plastic zone of the pore to undergo yielding while the surrounding material remains below the elastic threshold. Consequently, the stress drops in the plastic zone at the expense of higher plastic strain and the maximum stress shifts to the surrounding elastic region in the plane perpendicular to the loading axis. This shows that once the crack initiates, it will propagate in the plane perpendicular to the loading axis.

For a surface hemispherical pore, the stress and strain distribution were found to vary in the pore cross-section as one face is free (referred as the mouth of the pore) while the other face is constrained (referred as the root of the pore). This difference causes the load direction local strain to be higher at the mouth of the pore as shown Fig. 8(a), while the load direction local stress is higher at the root of the pore as shown in Fig. 8(b). The higher stress concentration at the root of the surface hemispherical pore will therefore lead to crack initiation at the pore root.

Fig. 9 shows the local cyclic stress-strain response in the region of maximum strain for each of the pore geometries. Due to the constrained boundary condition, the local stress-strain response at the root of an internal pore is very similar to that of the hemispherical surface pore (Figs. 9a, 9b, K_t = 2.08 and 2.10). The higher K_t for the internal oblate spherical pore leads to significantly higher cyclic plastic strain accumulation (Fig. 9c, K_t=2.5). Same statement can be made for the subsurface pore in Fig. 9d (K_t = 2.52).

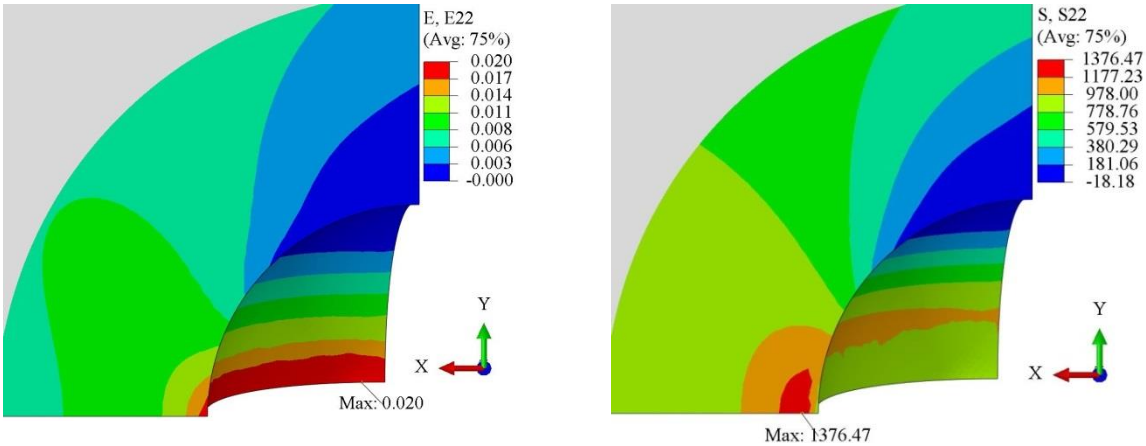

(a) Load direction strain (E22) (b) Load direction stress (S22) (MPa)

Fig. 8 Surface hemispherical pore (symmetry boundary in *X-Z*, *Y-X*; free boundary in *Z-Y*), (a) local strain is greatest at pore mouth indicated as "Max 0.02" (free boundary on one face), (b) local stress greatest at the pore root indicated as "Max 1376.47" (symmetric boundary condition on the adjacent faces); at applied maximum stress 750 MPa, applied stress ratio − 0.5.

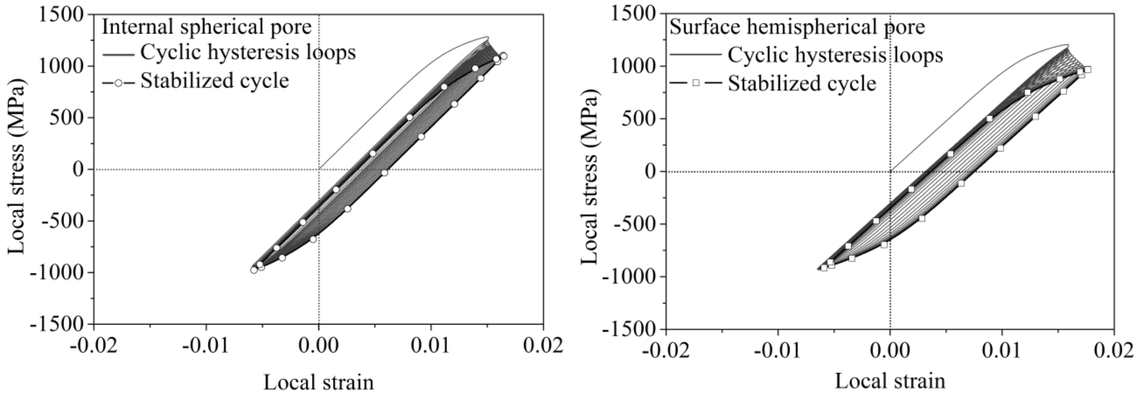

(a) (b)

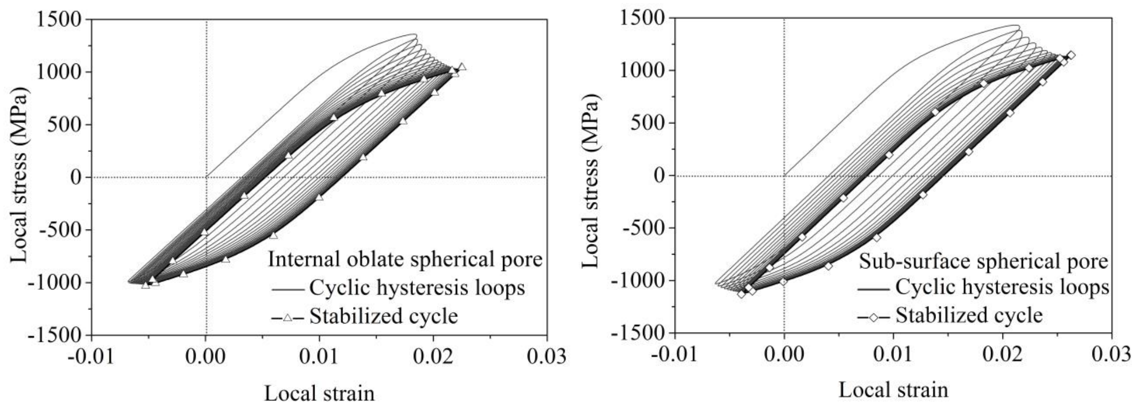

(c) (d)

Fig. 9. Local stress and strain responses at the root of (a) internal spherical pore, (b) surface hemispherical pore; (c) internal oblate spherical pore, (d) subsurface spherical pore at a distance of 0.2*d* from free surface, where *d* is the pore diameter; stable hysteresis loops established after 20 loading cycles with applied stress amplitude 560 MPa, applied stress ratio −0.5. Note the reduction in local stress ratio to nearly −1 owing to the stress concentration and cyclic plastic deformation.

(b) FEA vs. Neuber's method

Neuber's approach was also used to calculate the local stress and strain at the root of the three pore geometries. The FE model results were plotted against Neuber's results in Fig. 10 in terms of calculated local strain amplitude, under applied stress amplitudes between 200 MPa and 560 MPa with applied stress ratios of 0.1, −0.2 and −0.5. It was found that local strain obtained from FE model was in good agreement with Neuber's method for lower plastic strains. For higher plastic strains, Neuber's method was relatively conservative as compared to FE method. This is because Neuber's method is better suited for low plastic strains [40], whereas the advanced computation techniques in FE method have enabled us to implement complex algorithms to model the non-linear material response with a better approximation.

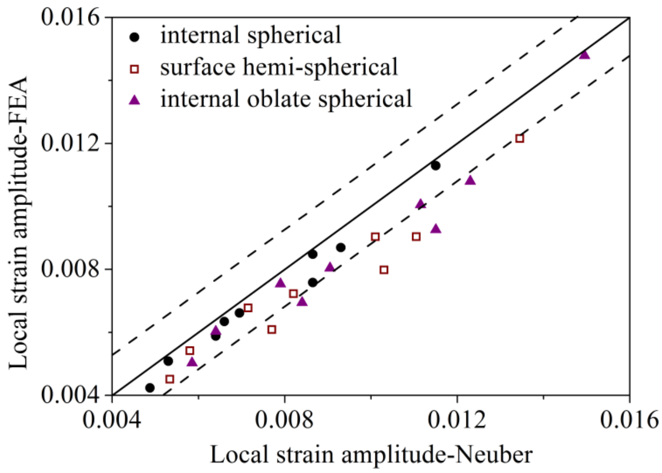

Fig. 10 Calculated local strain amplitudes: FEA vs. Neuber's method. Dotted lines indicate ±10% error.

4.3 Validation of predicted life with test results

Fatigue data reported in the literature with respective fracture surface images showing crack initiation at individual gas pores were used to validate the prediction model presented in Section 3. From the fracture surface images, the pore geometry, distance from free surface and the nearest idealised defect shape were determined for modelling. The present FE model does not account for the interaction between adjacent pores, therefore the test cases were selected with no other visible pores in the vicinity of the crack initiating pore. All the studies [6,20,21] reported the use of optimized processing parameters, which makes it highly likely that the distance between the pores is more than four times the pore diameter, which was determined by the FE model in this study to be the minimum distance for neglecting any interaction.

Summary of the porosity characteristics and experimental fatigue life [6,20,25] are presented in Table 4 along with the fatigue life prediction conducted in this study. The local strain obtained from

FE analysis was used in the SWT relationship, Eq. (13), to predict the fatigue life. Fig. 11 shows that the fatigue life prediction was in good agreement with the test data.

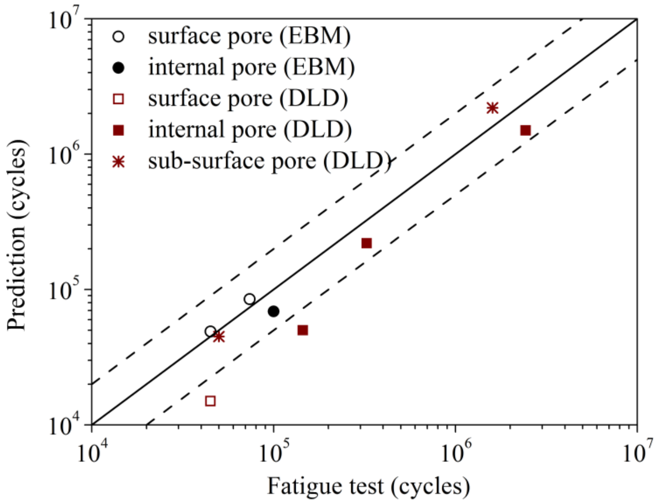

Fig. 11. Validation of the fatigue life prediction with the fatigue test data taken from literature as shown in Table 4. The dotted lines show the error bands of ±2 factor.

Table 4. Fatigue test data of AM Ti-6Al-4V specimens taken from literature with crack initiation at gas pores of known size, location and shape.

Initiating defect			AM process	Maximum applied stress (MPa)	Applied stress ratio	Fatigue life (prediction) (cycles)	Fatigue life (test) (cycles) [reference]
Location	Aspect ratio	Dia. (μm)					
Surface	1	72	EBM	575	0	8.5×10^4	7.34×10^4 [6]
Surface	1	70	EBM	600	0	4.9×10^4	4.5×10^4 [6]
Internal	1	170	EBM	600	0	6.9×10^4	1×10^5 [6]
Subsurface	1	45	DLD	356	−1	2.2×10^6	1.6×10^6 [20]
Subsurface	1	58	DLD	470	−1	1.5×10^4	4.5×10^4 [20]
Surface	1	100	DLD	415	−1	4.5×10^4	5×10^4 [20]
Internal	1	160-240	DLD	680	0.1	5×10^4	1.45×10^5 [21]
Internal	1		DLD	570	0.1	2.2×10^5	3.25×10^5 [21]
Internal	1		DLD	550	0.1	1.5×10^6	2.4×10^6 [21]

Note: Porosity-fatigue life data of reference [20] was provided by the authors via. email communications.

4.4 Parametric study

This section of the work is aimed at quantification of the fatigue strength reduction of powder-based AM Ti-6Al-4V in the presence of isolated gas pores. The ability of validated FE model for calculating the local stress and strain at the root of the porosity makes virtual testing an option to generate S-N curves for specimens containing isolated gas pores. Fig. 12 shows predicted S-N relationship for specimens with spherical gas pore defect (K_t = 2.08) at different applied stress ratios.

Similar exercise was also carried out for the surface hemispherical pore, internal oblate spherical pore, and the subsurface pore. For comparison, all the results from this parametric study were converted to applied stress ratio of −1 and plotted with the best-fit curve of HIPed AM Ti-6Al-4V in Fig. 13. The values of (σ_f', b) for the best-fit curve are (1630, −0.106) for internal spherical pore, (1701, −0.113) for surface hemispherical pore, (1466, −0.109) for oblate spherical pore and (1367, -0.109) for subsurface spherical pore at a distance of 0.2*d* below the free surface. Fig. 13 shows that the impact of porosity was less in the low cycle fatigue regime compared to the high cycle fatigue regime. This is because that as the applied stress increases the fatigue strength tends to converge towards the material static strength.

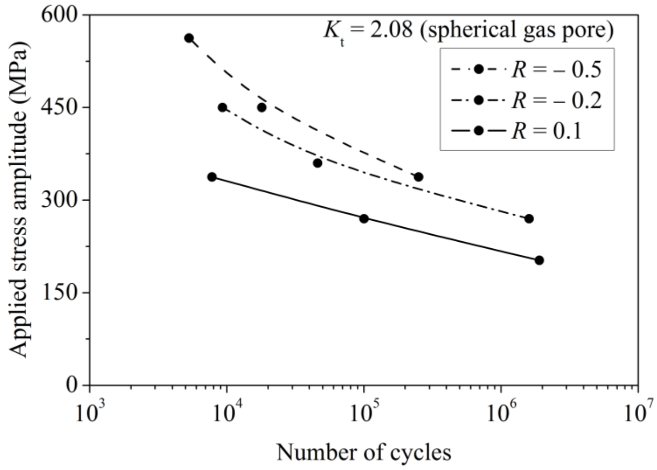

Fig. 12 Parametric study of the effect of applied stress amplitude and stress ratio on the fatigue life of the AM Ti-6Al-4V with an internal spherical gas pore.

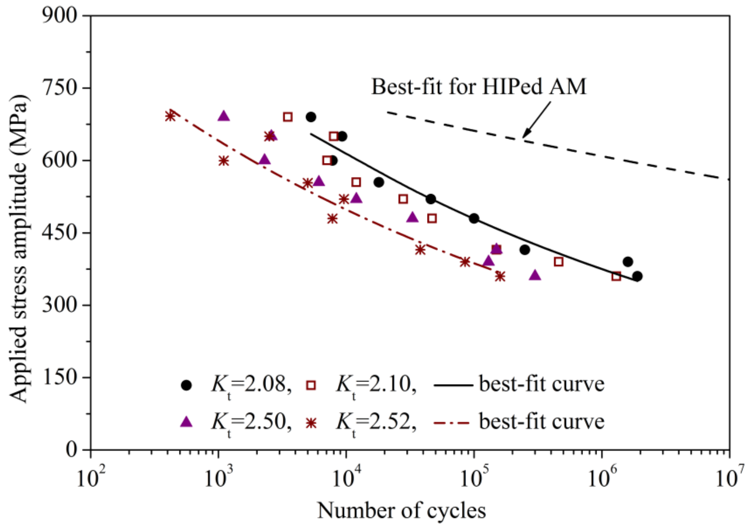

Fig. 13. Predicted S-N curves of AM Ti-6Al-4V containing isolated porosity compared with S-N data of HIPed AM Ti-6Al-4V, including internal spherical pore (K_t=2.08), surface hemispherical pore (K_t=2.1), internal oblate pore (K_t=2.5) and subsurface spherical pore at a distance of 0.2*d* to the free surface (K_t=2.52).

Fatigue performance of specimens with internal spherical gas pore and hemispherical surface pore was comparable for reasons discussed in Section 4. It should be noted that fatigue life predictions presented in Fig. 12 and Fig. 13 are for AM specimens that are built with optimised processing parameters (so that the assumption of scarcely distributed pores can be valid). However, if the distance between the pores is less than four times the diameter of the larger pore, then the interaction between pores should be considered. Therefore, the proposed S-N relationship can be used to determine the fatigue life of AM Ti-6Al-4V parts with isolated pores, which are built with optimized processing parameters and not subjected to hot isostatic pressing.

5. **Conclusions**

The effect of isolated porosity defects on the fatigue strength of AM Ti-6Al-4V material is evaluated based on the gas pore morphologies found in experiments. Elastic-plastic finite element analysis was performed first to calculate the cyclic plastic deformation, local stress and strains, and local mean stress change at the vicinity of the pores. The strain-life approach is used for the life prediction. S-N data of hot isostatically pressed AM Ti-6Al-4V are used as the benchmark for the material performance in its defect-free condition. Key findings are as follows.

1. Stress concentration factor (K_t) mainly depends on the location and shape of isolated gas pores. When the location of a spherical gas pore is more than four times of its diameter from the free surface, it is regarded as an internal defect and K_t is 2.08. For a subsurface spherical pore, K_t increases to the value range of 2.2 to 4.3 depending on the proximity to free surface. When the shape of internal pore change from spherical to oblate spherical with an aspect ratio of 2, K_t increases from 2.08 to 2.5.
2. The size of internal gas pore has little effect on the stress concentration factor, although larger pore contributes towards reduction in the load carrying cross-section area.
3. Plastic deformation at the pore root causes local mean stress relaxation. Using the local stress and strains from finite element analysis in the Smith-Watson-Topper strain-life equation can account for the effects of higher local strains and mean stress relaxation in the fatigue life prediction for AM Ti-6Al-4V specimens with gas pores.
4. The life prediction method is validated with published test results on powder based AM Ti-6Al-4V alloys, which has been further employed in parametric studies to understand the effect of porosity location and shape on the fatigue performance.

Acknowledgements

We are grateful to Coventry University for PhD studentship to Romali Biswal. We also thank Professor Nima Shamsaei and Dr Amanda J. Sterling for providing their fatigue test data for comparison and model validation.

References

[1] T. Debroy, H.L. Wei, J.S. Zuback, T. Mukherjee, J.W. Elmer, J.O. Milewski, A.M. Beese, A. Wilson-heid, A. De, W. Zhang, Progress in Materials Science Additive manufacturing of metallic components – Process , structure and properties, Prog. Mater. Sci. 92 (2018) 112–224. doi:10.1016/j.pmatsci.2017.10.001.

[2] B.H. Jared, M.A. Aguilo, L.L. Beghini, B.L. Boyce, B.W. Clark, A. Cook, B.J. Kaehr, J. Robbins, Additive manufacturing : Toward holistic design, Scr. Mater. 135 (2017) 141–147. doi:10.1016/j.scriptamat.2017.02.029.

[3] P. Edwards, M. Ramulu, Fatigue performance evaluation of selective laser melted Ti–6Al–4V, Mater. Sci. Eng. A. 598 (2014) 327–337. doi:10.1016/j.msea.2014.01.041.

[4] B.E. Carroll, T. A. Palmer, A.M. Beese, Anisotropic tensile behavior of Ti-6Al-4V components fabricated with directed energy deposition additive manufacturing, Acta Mater. 87 (2015) 309–320. doi:10.1016/j.actamat.2014.12.054.

[5] M. Kahlin, H. Ansell, J.J. Moverare, Fatigue behaviour of notched additive manufactured Ti6Al4V with as-built surfaces, Int. J. Fatigue. 101 (2017) 51–60. doi:10.1016/j.ijfatigue.2017.04.009.

[6] P.J. Tammas-Williams, S, Withers, I. Todd, P.B. Prangnell, The Influence of Porosity on Fatigue Crack Initiation in Additively Manufactured Titanium Components, Sci. Rep. (2017) 1–13. doi:10.1038/s41598-017-06504-5.

[7] J. Günther, D. Krewerth, T. Lippmann, S. Leuders, T. Tröster, A. Weidner, H. Biermann, T. Niendorf, Fatigue life of additively manufactured Ti-6Al-4V in the very high cycle fatigue regime, Int. J. Fatigue. 94 (2016) 236–245. doi:10.1016/j.ijfatigue.2016.05.018.

[8] G. Kasperovich, J. Hausmann, Improvement of fatigue resistance and ductility of TiAl6V4 processed by selective laser melting, J. Mater. Process. Technol. 220 (2015) 202–214. doi:10.1016/j.jmatprotec.2015.01.025.

[9] S. Leuders, M. Thöne, A. Riemer, T. Niendorf, T. Tröster, H.A. Richard, H.J. Maier, On the mechanical behaviour of titanium alloy TiAl6V4 manufactured by selective laser melting: Fatigue resistance and crack growth performance, Int. J. Fatigue. 48 (2013) 300–307. doi:10.1016/j.ijfatigue.2012.11.011.

[10] S. Tammas-Williams, P.J. Withers, I. Todd, P.B. Prangnell, Porosity regrowth during heat treatment of hot isostatically pressed additively manufactured titanium components, Scr. Mater. 122 (2016) 72–76. doi:10.1016/j.scriptamat.2016.05.002.

[11] M. Svensson. U. Ackelid, Additive manufacturing of dense metal parts by electron beam melting, ISBN: 9781615676361, Mater. Sci. & Tech. Conference, (2009) 2711–9.

[12] C. Qiu, G.A. Ravi, C. Dance, A. Ranson, S. Dilworth, M.M. Attallah, Fabrication of large Ti-6Al-4V structures by direct laser deposition, J. Alloys Compd. 629 (2015) 351–361. doi:10.1016/j.jallcom.2014.12.234.

[13] E. Brandl, U. Heckenberger, V. Holzinger, D. Buchbinder, Additive manufactured AlSi10Mg samples using Selective Laser Melting (SLM): Microstructure, high cycle fatigue, and fracture behavior, Mater. Des. 34 (2012) 159–169. doi:10.1016/j.matdes.2011.07.067.

[14] S. Leuders, M. Vollmer, F. Brenne, T. Tröster, T. Niendorf, Fatigue Strength Prediction for Titanium Alloy TiAl6V4 Manufactured by Selective Laser Melting, Metall. Mater. Trans. A. 46 (2015) 3816–3823. doi:10.1007/s11661-015-2864-x.

[15] Y. Murakami, Metal fatigue: Effects of Small Defects and Nonmetallic Inclusions, 1st ed., Elsevier, 2002.

[16] E. Wycisk, A. Solbach, S. Siddique, D. Herzog, F. Walther, C. Emmelmann, Effects of Defects in Laser Additive Manufactured Ti-6Al-4V on Fatigue Properties, Phys. Procedia. 56 (2014) 371–378. doi:10.1016/j.phpro.2014.08.120.

[17] S. Siddique, M. Imran, M. Rauer, M. Kaloudis, E. Wycisk, C. Emmelmann, F. Walther, Computed tomography for characterization of fatigue performance of selective laser melted parts, Mater. Des. 83 (2015) 661–669. doi:10.1016/j.matdes.2015.06.063.

[18] S. Timoshenko, J.N. Goodier, Theory of Elasticity, 2nd ed., (1951), 361-365. doi:10.1017/S036839310012471X

[19] D. Greitemeier, C. Dalle Donne, F. Syassen, J. Eufinger, T. Melz, Effect of surface roughness on fatigue performance of additive manufactured Ti–6Al–4V, Mater. Sci. Technol. 32 (2016) 629–634. doi:10.1179/1743284715Y.0000000053.

[20] A.J. Sterling, B. Torries, N. Shamsaei, S.M. Thompson, D.W. Seely, Fatigue behavior and failure mechanisms of direct laser deposited Ti-6Al-4V, Mater. Sci. Eng. A. 655 (2016) 100–112. doi:10.1016/j.msea.2015.12.026.

[21] D. Greitemeier, F. Palm, F. Syassen, T. Melz, Fatigue performance of additive manufactured TiAl6V4 using electron and laser beam melting, Int. J. Fatigue. 44 (2016) 211–217. doi:10.1016/j.ijfatigue.2016.05.001.

[22] S. Leuders, T. Lieneke, S. Lammers, T. Tröster, T. Niendorf, On the fatigue properties of metals manufactured by selective laser melting – The role of ductility, J. Mater. Res. 29 (2014) 1911–1919. doi:10.1557/jmr.2014.157.

[23] N. Hrabe, T. Gnaupel-Herold, T. Quinn, Fatigue properties of a titanium alloy (Ti-6Al-4V) fabricated via electron beam melting (EBM): Effects of internal defects and residual stress, Int. J. Fatigue. 94 (2015) 202–210. doi:10.1016/j.ijfatigue.2016.04.022.

[24] S. Bagehorn, J. Wehr, H.J. Maier, Application of mechanical surface finishing processes for roughness reduction and fatigue improvement of additively manufactured Ti-6Al-4V parts, Int. J. Fatigue. 102 (2017) 135–142. doi:10.1016/j.ijfatigue.2017.05.008.

[25] Y.M. Hiroshige Masuo, Yuzo Tanaka, Shotaro Morokoshi, Hajime Yagura, Tetsuya Uchida, Yasuhiro Yamamoto, Effects of Defects , Surface Roughness and HIP on Fatigue of Ti-6Al-4V manufactured by Additive Manufacturing, Procedia Struct. Integr. 7 (2017) 19–26. doi:10.1016/j.prostr.2017.11.055.

[26] D. Agius, K.I. Kourousis, C. Wallbrink, T. Song, A Cyclic plasticity and microstructure of as-built SLM Ti-6Al-4V : The effect of build orientation, Mater. Sci. Eng. A. 701 (2017) 85–100. doi:10.1016/j.msea.2017.06.069.

[27] A. Phaiboonworachat, K.I. Kourousis, Cyclic elastoplastic behaviour, hardness and microstructural properties of Ti-6Al-4V manufactured through selective laser melting, Int. J. Mater. Eng. Innov. 7 (2016) 80–87. doi:10.1504/IJMATEI.2016.077324.

[28] A.A. Antonysamy, Microstructure, Texture and Mechanical Property Evolution during Additive Manufacturing of Ti-6Al-4V Alloy for Aerospace Applications, PhD thesis, Manchester University, 2012.

[29] B. Dutta, V. Singh, H. Natu, J. Choi, J. Mazumder, Direct Metal Deposition, Adv. Mater. Process. 167 (2009) 33–36. http://mbraun.com/images/201/POM Group.pdf.

[30] T. Vilaro, C. Colin, J.D. Bartout, As-fabricated and heat-treated microstructures of the Ti-6Al-4V alloy processed by selective laser melting, Metall. Mater. Trans. A Phys. Metall. Mater. Sci. 42 (2011) 3190–3199. doi:10.1007/s11661-011-0731-y.

[31] G. Lutjering, J.C Williams, Titanium, 2nd ed., 2007.

[32] H. Galarraga, D. A. Lados, R.R. Dehoff, M.M. Kirka, P. Nandwana, Effects of the microstructure and porosity on properties of Ti-6Al-4V ELI alloy fabricated by electron beam melting (EBM), Addit. Manuf. 10 (2016) 47–57. doi:10.1016/j.addma.2016.02.003.

[33] P. Li, D.H. Warner, A. Fatemi, N. Phan, Critical assessment of the fatigue performance of additively manufactured Ti-6Al-4V and perspective for future research, Int. J. Fatigue. 85 (2016) 130–143. doi:10.1016/j.ijfatigue.2015.12.003.

[34] M. Simonelli, Microstructure evolution and mechanical properties of Selective Laser Melted Ti-6Al-4V, PhD thesis, Loughborough University, 2014.

[35] A. Thant, Y. Miyashita, Y. Otsuka, Y. Mutoh, S. Sakurai, Notch fatigue behavior of Ti-6Al-4V alloy in transition region between low and high cycle fatigue, Int. J. Fatigue. 95 (2017) 194–203. doi:10.1016/j.ijfatigue.2016.10.024.

[36] R.W. Hertzberg, Deformation and fracture mechanics of engineering materials, 4th ed., Wiley, 1989.

[37] R. Cunningham, A. Nicolas, J. Madsen, E. Fodran, M.D. Sangid, A.D. Rollett, Analyzing the effects of powder and post- processing on porosity and properties of electron beam melted Ti-6Al-4V, Mater. Res. Lett. 5 (2017) 516–525. doi:10.1080/21663831.2017.1340911.

[38] Metallic Materials Properties Development and Standardization, MMPDS-04, (2008).

[39] Models for metals subjected to cyclic loading Products: Abaqus/Standard Abaqus/Explicit Abaqus/CAE, Abaqus Doc. (n.d.) 1–11.

[40] R. I. Stephens, A. Fatemi, R. R. Stephens, H. O. Fuchs, Metal Fatigue in Engineering, 2nd ed., John Wiley and sons, 2000.

[41] P. Sergio, C. Pereira, L.C. Campanelli, C. Adolfo, E. Claros, T. Ferreira, D.P. Oliveira, C. Bolfarini, Prediction of the surface finishing roughness effect on the fatigue resistance of Ti-6Al-4V ELI for implants applications, Int. J. Fatigue. 103 (2017) 258–263. doi:10.1016/j.ijfatigue.2017.06.007.

[42] K.N. Smith, P. Watson, T.H. Topper, A stress-strain function for the fatigue of metals, J. Mater. 5 (1970) 767–778.

[43] R.A. Eubanks, Stress concentration due to a hemispherical pit at a free surface, Technical report, Illinois Institute of Technology, 1953.

[44] W.D. Pilkey, D.F. Pilkey, Peterson’s Stress Concentration Factors, 3rd ed., 2008. doi:10.1002/9780470211106.